Large-amplitude plasma waves and $2\omega_p$ emission driven by laser-generated electron jets in overdense plasma layers

TH. KUNZL, R. LICHTERS, AND J. MEYER-TER-VEHN

Max-Planck-Institut für Quantenoptik, Garching, Germany

Abstract

The excitation of large-amplitude plasma waves by intense few-cycle laser pulses in thin overdense plasma layers is studied using one-dimensional particle-in-cell simulation. *P*-polarized pulses generate relativistic electron pulses (jets) at the irradiated surface that penetrate the layer and then oscillate back and forth due to reflection by self-generated space charge fields building up in front of the surfaces. Counterpropagating plasmons of large amplitude are excited and start to emit radiation at $2\omega_p$ and other harmonics of the plasma frequency. The analogy to type III solar radio emission that is driven by electron bursts from deeper layers of the solar corona is pointed out; it highlights the present topic as another example of laboratory astrophysics with lasers.

Keywords: $2\omega_p$ radiation; Few-cycle laser pulses; Large amplitude plasma waves; Relativistic electron jets

1. INTRODUCTION

High-power lasers provide possibilities to study different aspects of astrophysical phenomena in the laboratory (Remington *et al.*, 2000; Ryutov *et al.*, 2001). Recent advances in generating ultrashort laser pulses with intensities far beyond 10^{18} W/cm^2 (Strickland & Mourou, 1985; Mourou *et al.*, 1998) allow us to access new regimes of relativistic electron beams (REB) carrying huge currents and magnetic fields (Pukhov & Meyer-ter-Vehn, 1996; Tatarakis *et al.*, 2002). Here we study the excitation of large-amplitude plasma waves (Langmuir waves) by laser-generated relativistic electron beams and their emission of electromagnetic radiation at multiples of the plasma frequency. Such emission was discussed long ago (Aamodt & Drummond, 1964); it has been observed in solar type III radio bursts where two bands of emission are found that are interpreted as fundamental and second harmonic plasma emission driven by Langmuir waves (e.g., Melrose *et al.*, 1986). The detailed models for the ratio of fundamental and harmonic emission and the absolute intensities are still under discussion (e.g., Vasquez *et al.*, 2002).

The two configurations of the laser experiment and the solar corona are sketched in Figure 1. Different REB sources have been used to make plasma waves in the laboratory (Vyacheslavov *et al.*, 2002). Here we investigate a *p*-polarized laser pulse focused to relativistic intensity on a thin over-dense plasma layer (see Fig. 1a). With the period of the laser light, it produces electron pulses that start to oscillate through the foil. They have current densities of the order of 10^{12} A/cm^2. The pulses generate counterpropagating plasmons and subsequent radiation at multiples of the plasma frequency. This process will be described in detail below.

In the solar case (see Fig. 1b), these energetic electrons are generated near the solar surface by magnetic reconnection, a process releasing energy of a twisted magnetic field by sudden reconnection of the magnetic field lines. Small scale magnetic fields near the solar surface are constantly twisted as the sun rotates differentially. Reconnection events on small time and space scales take place frequently and are stochastically distributed. The fast electron beams move through the coronal plasma and excite Langmuir waves triggered by two-stream instability. An important point is that the waves are first created in a forward direction, but quickly scatter on ion polarization clouds so that the growth rate of the instability is strongly reduced. This leads to an almost isotropic distribution of Langmuir waves in the excitation region, which is believed to extend over 2 solar radii or 1.4 million km.

The radio emission occurs when two or more plasmons decay into a photon. The simplest process is two-plasmon decay obeying the matching conditions

$$\omega_1 + \omega_2 = \omega_T \approx 2\omega_p,$$

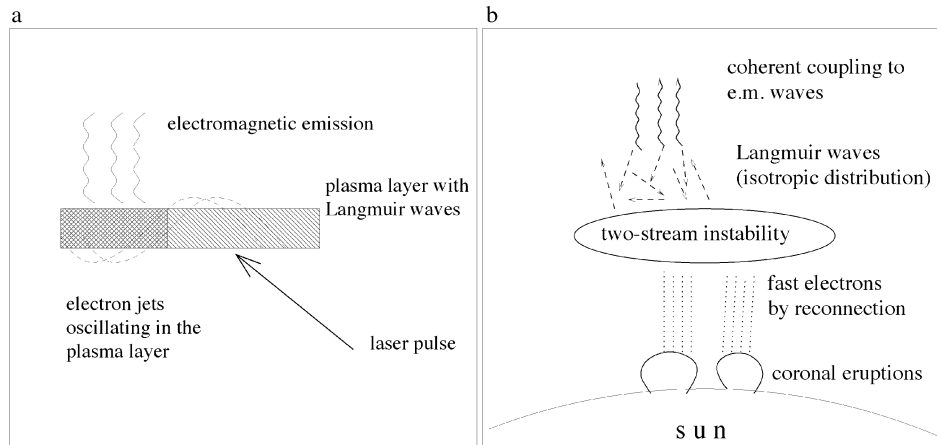$$\boldsymbol{k}_1 + \boldsymbol{k}_2 = \boldsymbol{k}_T, \tag{1}$$

Fig. 1. a: Schematic drawing of the laboratory configuration investigated in this article. b: Schematic picture of the standard model for solar type III radio bursts.

where $\omega_p = 4\pi e^2 n_0/m$ is the plasma frequency with electron density n_0, charge e, and mass m of the electron. Because the plasmon wave vectors $\boldsymbol{k}_1$ and $\boldsymbol{k}_2$ are typically much larger than the photon wave vector $\boldsymbol{k}_T$, they have to be approximately antiparallel, implying counterpropagating waves. The photon energy is $\omega_T \approx 2\omega_p$. Higher order processes involving more plasmons may lead to radiation also at other multiples of ω_p. When probing the sun in the radio frequency range, one observes transient features of coherent radio emission. The signal starts at a frequency of about 100 MHz and stays on for some 10 s, during which the frequency gradually declines. In many cases, a second frequency band of almost equal intensity can be traced, which suggests that the two bands represent emission at the fundamental and the second harmonics of the plasma frequency. The decreasing frequency indicates that the radiation source travels outward in the solar corona into regions of lower electron density and therefore smaller plasma frequency. The measured time scales are consistent with such a picture, taking the source as a beam of mildly relativistic electrons with a velocity of about 40% of the speed of light.

Experimental evidence for $2\omega_p$ emission from laser-irradiated materials has been reported (Teubner *et al.*, 1997), but more experimental work seems necessary to substantiate these results. The intention of the present article is to give a basis for such experiments by means of one-dimensional particle-in-cell (1D PIC) simulation, using the code LPIC++ (Lichters *et al.*, 1997). First results of this work had been reported in 1998 (Lichters *et al.*, 1998). It uses kinetic simulation of laser plasma interaction at the target surface, describing hot electron transport through the foil, plasmon excitation by two-stream instability, and two-plasmon decay into photons.

The simulation considers only one spatial dimension (i.e., all physical quantities depend on x and t, but not on y or z). However, it takes into account all three velocity components, and therefore allows us to treat oblique incidence of arbitrarily polarized laser beams. Oblique incidence is treated by transforming into a boosted frame in which the laser beam is normally incident on a moving foil. Details of this Lorentz transformation are described in Section 2 and the evolution of electron phase space in Section 3. Section 4 is devoted to an analysis of plasmon distributions in x, t space and k, ω space and their decay into photons at multiples of the plasma frequency. In Section 5, the $2\omega_p$ emission is treated analytically on the basis of the cold fluid approximation.

The restriction to one spatial dimension represents a severe limitation of the present treatment for two reasons. First, it excludes surface plasma waves that are certainly also excited and couple through nonlinear terms to the electromagnetic spectrum (Ivanov & Ryutov, 1965; Ryutov, 1966). Second, the transverse distribution of laser intensity and light pressure over a focus of finite size leads to crater formation, destroying the planar target geometry. Third, the fast electron current driven into the foil is subject to transverse Weibel instability, leading to current filamentation, which cannot be described in the present 1D treatment. These phenomena clearly show up in 2D and 3D PIC simulation (see, e.g., Pukhov & Meyer-ten-Vehn, 1997; Honda *et al.*, 2000). To mitigate these effects, we restrict the present investigation to very short, few-cycle laser pulses, which have now become available experimentally (Brabec & Krausz, 2000), and consider configurations with a focal diameter large relative to target thickness, in which planar geometry should prevail over a longer period. The influence of current filamentation with a spatial scale of c/ω_p on plasmon excitation is more difficult to judge and certainly needs future multidimensional investigation. Nevertheless, we believe that the present 1D results give a qualitatively valid picture and a basis for stimulating experiments.

2. OBLIQUE LASER INCIDENCE IN 1D DESCRIPTION

The numerical results shown in the subsequent sections have been obtained with the 1D PIC code LPIC++. This code is documented and freely available (Lichters *et al.*, 1997). The

code simulates the interaction of strong, ultrashort laser pulses with thin plasma layers and allows for a self-consistent treatment of electrostatic and electromagnetic waves. Oblique incidence of the laser pulse is included in this 1D description by means of a Lorentz transformation into a moving frame, in which the light is normally incident on the layer (Bourdier, 1983). This transformation is possible because the code considers three velocity and field components, though only one spatial coordinate. It also allows us to study arbitrary polarization. In the present simulations, the material layer is assumed to be fully ionized initially.

The interaction of the laser pulse with the plasma layer is treated in the frame L′ illustrated in Figure 2. For *p*-polarized light, only the propagation direction *x* and the polarization direction *y* are of importance. The wave vector of the incident light in the laboratory system L

$$\begin{pmatrix} \omega_0/c \\ k_x \\ k_y \end{pmatrix} = k_0 \begin{pmatrix} 1 \\ \cos\alpha \\ \sin\alpha \end{pmatrix} \quad (2)$$

transforms to the moving system L′ according to

$$\begin{pmatrix} \omega'/c \\ k'_x \\ k'_y \end{pmatrix} = \begin{pmatrix} \Gamma(\omega_0/c - \beta k_y) \\ k_x \\ \Gamma(-\beta\omega_0/c + k_y) \end{pmatrix}, \quad (3)$$

where $\Gamma = \sec\alpha$ is the Lorentz factor corresponding to the velocity $\beta = v_y/c$ of the frame in positive *y* direction. For $\beta = k_y c/\omega_0 = \sin\alpha$, one has

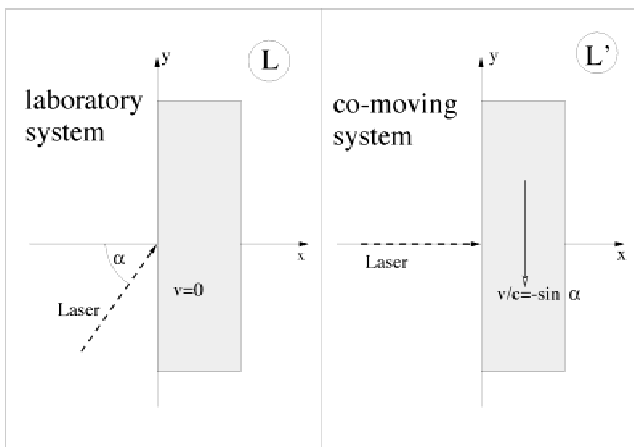$$\omega' = \omega_0 \cos\alpha$$

$$k'_x = k_0 \cos\alpha$$

$$k'_y = 0.$$

Fig. 2. Schematic view of the simulation geometry for a *p*-polarized laser pulse. In the laboratory system L the target plasma is at rest, and the laser pulse is incident under an angle of α; in system L′ the plasma moves uniformly with velocity $v/c = -\sin\alpha$ in *y* direction such that the laser shines on the foil perpendicularly.

In this boosted frame, the 1D laser plasma equations in the cold fluid approximation have the form (Lichters, 1997)

$$\left(\partial_x^2 - \frac{1}{c^2}\partial_t^2\right)a_y = \left(\frac{\omega_p}{c}\right)^2\left[\frac{n}{\gamma\cos\alpha}(a_y - \tan\alpha) + \tan\alpha\right], \quad (4)$$

$$\gamma\cos\alpha = \sqrt{\frac{1 + (a_y\cos\alpha)^2 - a_y\sin(2\alpha)}{1 - \beta_x^2}}, \quad (5)$$

$$\partial_x^2\phi = \left(\frac{\omega_c}{c}\right)^2\frac{1}{\cos\alpha}(n-1), \quad (6)$$

$$0 = \partial_t n + c\partial_x(n\beta_x) \quad (7)$$

$$d_t\beta_x = \frac{c}{\gamma}(1 - \beta_x^2)\partial_x\phi$$

$$-\frac{1}{\gamma^2}(c\partial_x + \beta_x\partial_t)\left(\frac{a_y^2}{2} - a_y\tan\alpha\right), \quad (8)$$

where we used normalized quantities for the amplitude of the vector potential $a_y = eA_y/(mc^2)$, the electron density $n = n_e/n_0$, the electrostatic potential $\phi = e\Phi(mc^2)$, and the *x* component of the fluid velocity $\beta_x = v_x/c$. Here we have assumed *p*-polarized light, that is, $a_x = 0$. In linear approximation, these equations allow for electrostatic (Langmuir) waves

$$\phi_1(x,t) = \phi_0\sin(\omega t - kx)$$

$$a_{y1}(x,t) = -\phi_1(x,t)\sin\alpha$$

$$n_1(x,t) = -\phi_1(x,t)(ck/\omega_p)^2\cos\alpha$$

$$\beta_{x1}(x,t) = -\phi_1(x,t)(ck/\omega_p)\cos^2\alpha \quad (9)$$

with $\omega = \omega_p\cos\alpha$ and arbitrary *k*. In addition, light waves

$$a_{y1}(x,t) = a_0\sin(\omega t - kx) \quad (10)$$

$$\phi_1(x,t) = (\omega_p/ck)^2\sin\alpha\, a_{y1}(x,t), \quad (11)$$

can propagate with the usual dispersion relation $\omega^2 = \omega_p^2 + (ck)^2$. Notice that, in the boosted frame, the fields $a_y(x,t)$ and $\phi(x,t)$ are coupled to each other such that, for example, electrostatic waves are not purely longitudinal, but have an E_y component for $\alpha > 0$.

The code LPIC++ solves the set of nonlinear Eqs. (4) numerically. In this article, we present simulations of a *p*-polarized laser pulse incident under an angle of $\alpha = 55°$ on a plane layer of overcritical, fully ionized plasma with sharp boundaries. The angle is chosen to optimize $2\omega_p$ emission (see Section 4). The pulse shape is

$$a_y(s) = \Theta(t/\tau)\Theta((T-t)/\tau)a_0\sin\left(2\pi\frac{s}{2T}\right)\sin(\omega_0 s), \quad (12)$$

with $s = t - x/c$, $\tau = 2\pi/\omega_0$, and $\Theta(x)$ is the Heaviside step function. A short pulse $T = 4\tau$ is chosen. The plasma density

is $n_0 = 18 n_c$, where $n_c = \pi m c^2 / (e^2 \lambda_0^2)$ is the critical density and $\lambda_0 = 2\pi c/\omega_0$ the laser wavelength. two layer thicknesses d are considered:

- $d = 1\lambda_0$ (the "thin foil" case) and
- $d = 5\lambda_0$ (the "thick foil" case).

The laser amplitude is taken as $a_0 = 2$ in both cases and corresponds to an intensity of $I = 5.5 \times 10^{18}$ W/cm^2 for 1-μm laser wavelength.

3. GENERATION OF FAST ELECTRONS

The laser pulse itself cannot penetrate into the overcritical plasma layer. The excitation of plasma waves inside the layer is mediated by fast electrons, which are accelerated to relativistic energies by the laser field at the surface. For a *p*-polarized laser pulse obliquely incident on a plasma surface, there are two mechanisms that drive the fast electrons:

- The light pressure normal to the surface that originates from the $\boldsymbol{v} \times \boldsymbol{B}$ force; it is of second order in the light amplitude and therefore oscillates with twice the laser frequency;
- The direct action of the laser electric field normal to the foil that pulls electrons off the surface, accelerates and reinjects them into the plasma periodically at laser frequency (vacuum heating; Brunel, 1987). This force is linear in the laser amplitude and is therefore the dominant process for laser intensities up to 10^{18} W/cm^2.

Different groups of fast electrons (called *jets* in the following) are observed in the phase space plots of Figures 3–6, showing v_x and v_y distributions in the laboratory system. In
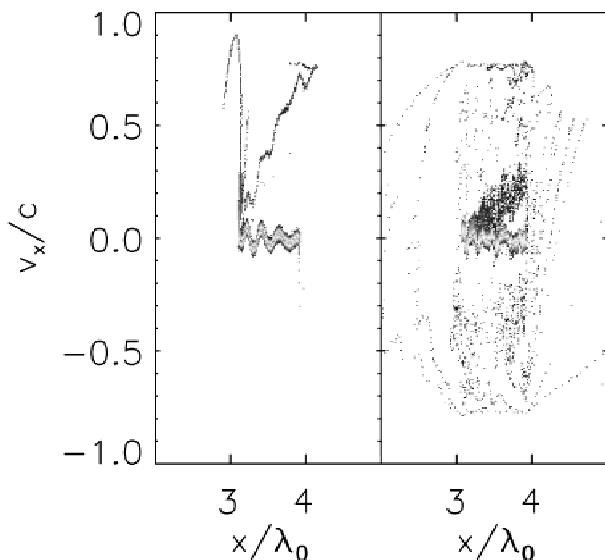
Fig. 4. Same as Figure 3, but for v_y.

Figure 3, v_x is plotted versus x for a plasma layer located at $3 < x/\lambda_0 < 4$. The fast electrons are generated close to the surface and disperse according to their velocity spectrum when penetrating into the plasma layer. After 4 laser periods (left side of Fig. 3), one observes a first jet that has spread over the full layer thickness and a second one just being formed at the left surface. Bulk plasma electrons at low velocity are seen to carry a large-amplitude plasma wave. Apparently, the first jet has excited this wave, which is acting back on the jet, modulating its velocity spectrum. After eight laser periods (right side of Fig. 3), the phase

Fig. 3. Phase space diagrams of electron velocity v_x for a 1λ-thick foil with $n/n_c = 18$ and a laser pulse incident from the left with $a_0 = 2$ and $\alpha = 55$ after $t/\tau = 4$ (left side) and $t/\tau = 8$ (right side) laser periods. While all high-velocity electrons are plotted, those belonging to the bulk plasma with high electron density are partially suppressed.
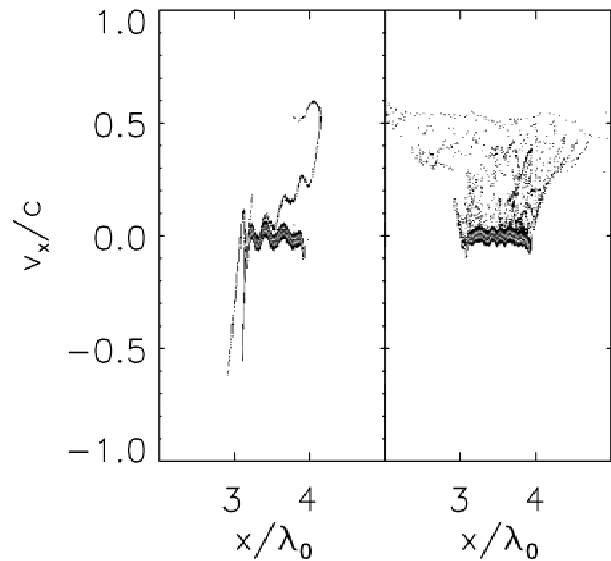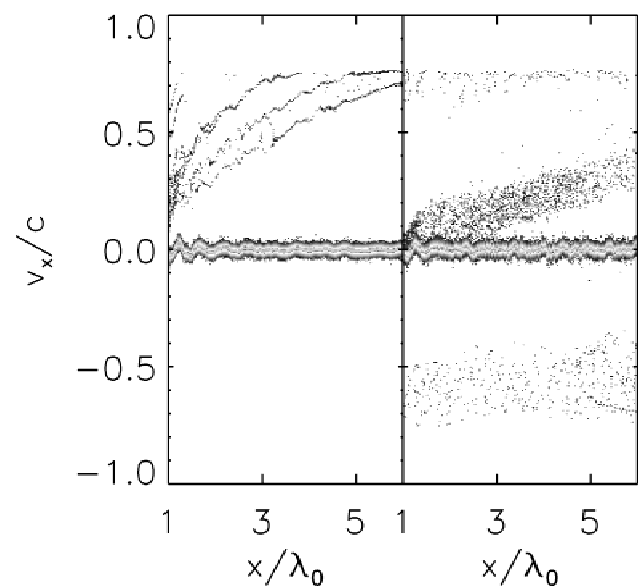
Fig. 5. Phase space diagrams for v_x for a $5\lambda_0$-thick foil after $t/\tau = 6$ (left side) and $t/\tau = 15$ (right side); plasma and laser parameters are the same as in Figure 3, and τ is the laser period.
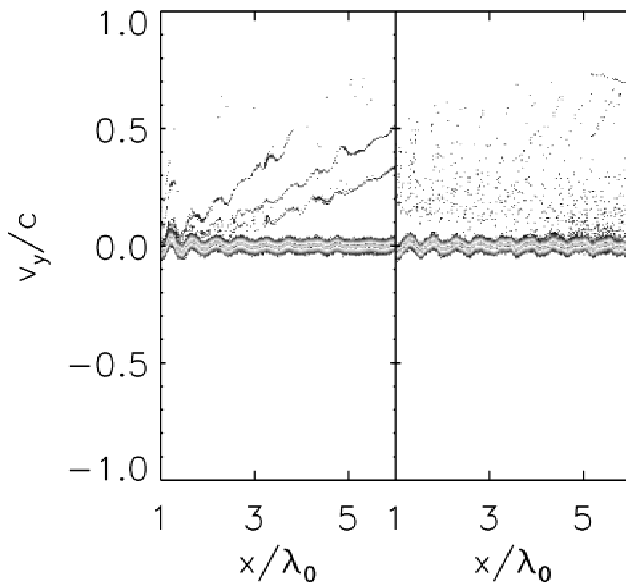
Fig. 6. Same as Figure 5, but for v_y.

Fig. 7. Electron density $n(x, t)$ plotted in x, t plane. Inside the foil, the gray scale has been selected to highlight the density oscillations around the initial density $n/n_c = 18$ in the range of $n_e/n_c = 14$–20. To also visualize laser-driven electrons of much lower density escaping the layer on both sides, each cell in this region with $n/n_c < 80$ has been indicated by a black dot except for cells with zero density, which remain white.

space looks more complicated. One now observes fast electrons at $x/\lambda_0 > 4$ beyond the right surface, where they build up a negative charge cloud, and electrons with $v_x < 0$, which have been reflected by this space charge and are now running from left to right. In addition, we recognize a dense band of electrons with velocities $v_x > 0$ in a range $v_x/c \approx$ 0.05–0.25. It appears that this electron group has also been heated by the peak of the laser pulse, but in deeper parts of the skin layer leading to a broader distribution at lower velocity as compared to the jet electrons.

In Figure 4, the corresponding v_y versus x plots are shown. Different from v_x, only electrons with positive v_y component are found inside the layer. This is a consequence of the oblique laser incidence. Inside the layer, the vector potential *analysis* vanishes, and the transverse electron momentum in the moving frame is

$$p'_y = -\beta'_y / \sqrt{1 - \beta'^2_x - \beta'^2_y} = -\tan\alpha, \qquad (13)$$

where β'_x and β'_y are the velocity component in L'. Using the relations $\beta'_y = (\beta_y - \beta)/(1 - \beta_y\beta)$, $\beta'_x = \beta_x\sqrt{1 - \beta^2}/(1 - \beta_y\beta)$ for the velocity transformation between the frames L' and L with relative velocity $\beta = \sin\alpha$, one obtains for the laboratory velocities

$$\beta_x = \pm\sqrt{2\beta_y\beta - (1 + \beta^2)\beta_y^2}$$

$$\beta_y = \left(1 \mp \sqrt{1 - \beta_x^2(1 + \beta^2)}\right)\beta/(1 + \beta^2), \qquad (14)$$

showing that $v_y > 0$ for $\alpha = 55°$. Equations (14) also imply upper limits for β_x and β_y depending on α. For $\alpha = 55°$, one finds $\beta_x \leq 0.774$ and $\beta_y \leq 0.819$, which is in good agreement with the maximum velocities seen in the phase space plots.
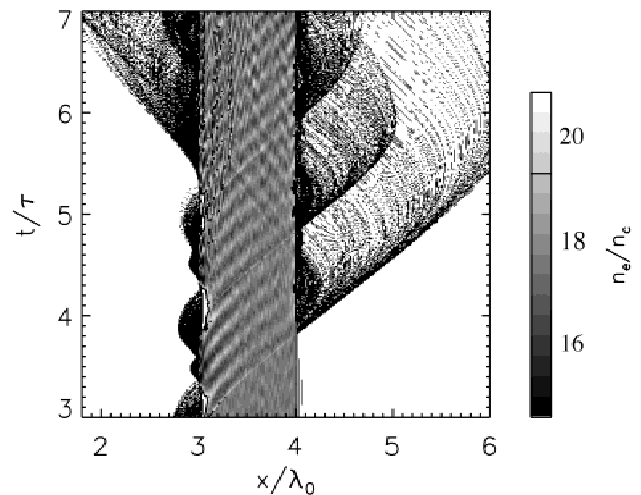
Some aspects of the electron evolution discussed above appear even more pronounced for a thicker layer with $d = 5\lambda_0$, leaving all other parameters unchanged. This is shown in Figures 5 and 6. At time $t = 6\tau$, one now sees three jet and the onset of a fourth one without interference of reflected electrons, as the jet travel time through the layer is longer. Reflected electrons populating the $v_x < 0$ plane are seen on the right side of Figures 5 and 6, showing the phase space at $t = 15\tau$. At this later time, one also very clearly observes the band of medium velocity electrons, clearly separated in phase space from both jet and plasma electrons.

The electron density $n(x, t)$ corresponding to the thin layer plots in Figures 3 and 4 is shown in Figure 7. It refers to the laboratory frame. The gray scale applies to the density inside the layer, while fast electrons outside the plasma are marked by black dots. The plot shows impressively the electron excitation by the laser pulse. At early times, one should notice the electrons pulled out from the irradiated left surface and then reinjected into the layer with period τ. Superimposed on the direct action of the laser electric field is the action of the ponderomotive pressure with the period $\tau/2$. The electrons pass the layer and emerge from the right-hand side. Due to space charge build-up, they cannot escape from the layer in large amounts, but rather return and then oscillate back and forth through the layer, where they excite plasma waves seen as density ripples inside the layer. Notice that also the electron group of intermediate velocity excites plasma waves, weakly seen as steep lines in Figure 7. The steepness corresponds to lower phase velocity.

The density profile is also plotted in Figure 8 as a snapshot at time $t = 5\tau$, showing details of the space charge distribution in front of the rear surface. Here the electron
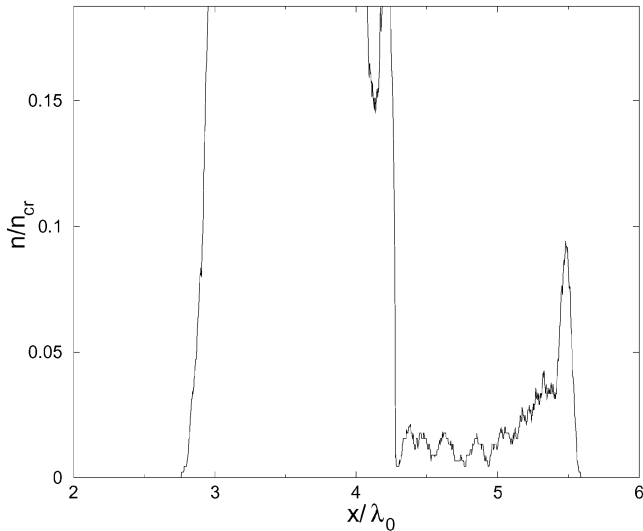
Fig. 8. Electron density $n(x,t)$ plotted versus x for $t = 5\tau$. The scale has been chosen to show the density distribution in front of the rear surface; notice that it is modulated with the plasma wave period.
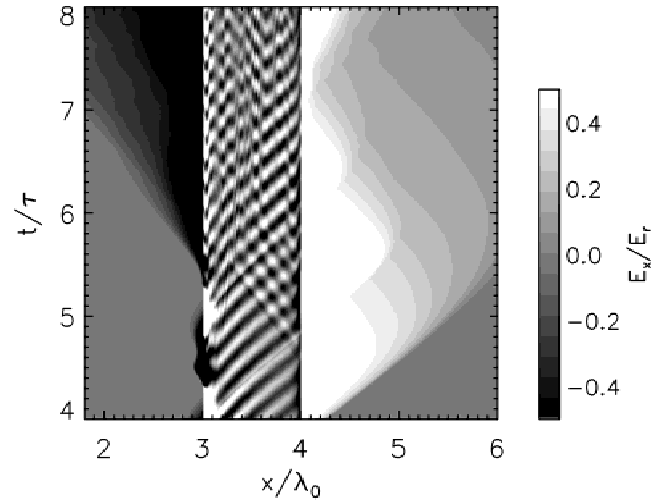

Fig. 9. The longitudinal electric field $E_x(x,t)/E_0$ plotted in the x,t plane, normalized to $E_0 = m_e\omega_p c/e$. The oblique lines in the plasma layer correspond to plasma waves, propagating to the right at early times during laser beam incidence ($t < 5\tau$) and in both directions later on. Another group of plasma waves having a much smaller phase velocity is indicated by weaker steep lines originating from the irradiated surface for $t > 4\tau$. Space charge fields of opposite polarity are seen in front of both surfaces.

density amounts typically to 2% of the critical density and reaches 10% at the right border.

4. PLASMON GENERATION AND RADIATION AT MULTIPLES OF ω_p

In this section, we study the evolution of plasma waves (plasmons) and their decay into photons at multiples of ω_p. The configuration of the laser-generated relativistic electron jet propagating on the background of a low-temperature plasma is two-stream unstable. Plasma waves grow from fluctuations under these conditions with phase velocities close to the maximum velocity of jet electrons (Lichters, 1997). They are best visualized by plotting the longitudinal electric field $E_x(x,t)$ in the x,t plane, as is shown in Figure 9. Here the gray scale reaches from black (large negative values) to white (large positive values); maximum values of $\pm 0.5E_0$ are obtained, where $E_0 = m_e\omega_p c/e$. Although the simulations are performed in the boosted frame L' (compare Sec. 2) in terms of the transformed quantities x', t', E_x', the normalized values shown in Figure 9 refer to the laboratory system. It should be clear that in the laboratory system, the plasmons move in the direction of the electron jets, and therefore have also an E_y component, corresponding to a wave-vector $\mathbf{k} = (k_x, k_y)$ with $k_y \neq 0$.

In Figure 9, the plasma wave structure is clearly visible inside the plasma layer located at $3 < x/\lambda_0 < 4$. Phase velocities vary somewhat as a function of x, but are generally close to c within a margin of $\pm 25\%$. Fourier transform of $E_x(x,t)$ has been performed both in space and time, and the transformed field $\widetilde{E}_x(k,\omega)$ is depicted in Figures 10 and 11 for different time windows. Due to reflection symmetry, $E_x(x,t) = E_x(-x,-t)$, the Fourier amplitude $\widetilde{E}_x(k,\omega)$ is real; for $\omega \approx \omega_p > 0$, we can distinguish between $k > 0$ and

$k < 0$ regions corresponding to right-bound and left-bound plasmons, respectively. In Figure 10, the early time window $2 < t/\tau < 5$ has been chosen, in which plasmons only travel from left to right, driven by the electron jets generated by laser incidence on the left-hand surface during this time (compare Fig. 9). Accordingly, only right-bound plasmon excitation with $\omega \approx \omega_p$ and $k > 0$ is found in Figure 10. Recall that $\omega_p/\omega_0 = \sqrt{n_e/n_c} = 4.24$ in the present case. The
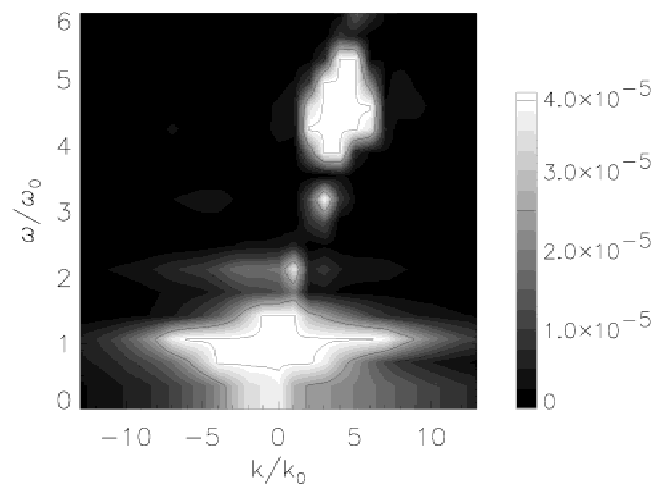

Fig. 10. Fourier transform $\widetilde{E}_x(k,w)$ of the electrostatic field $E_x(x,t)$ plotted in a k, ω plane in arbitrary units. This plot refers to an early stage of the simulation ($t/\tau = 2\ldots5$). The levels of the three contour lines are indicated on the gray scale. The large white peak around $\omega \approx \omega_0$ stems from surface oscillations driven at laser frequency, whereas the peak around $\omega/\omega_0 \approx 4.3$ is generated by right-going plasmons.
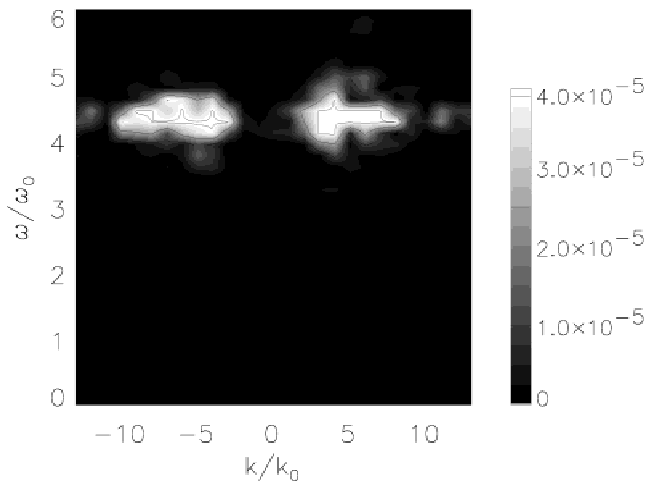
Fig. 11. Same as Figure 10, but for the later time window $6 < t/\tau < 12$, when the electron jets have been reflected and plasma waves run in both directions, having $k > 0$ and $k < 0$ wave vectors.

Fig. 12. Simulated spectrum of *p*-polarized electromagnetic radiation emitted from the rear surface (full line, transmitted light) and from the irradiated front side (broken line, reflected light). The spectrum corresponds to the electromagnetic field recorded during the time period $9 < t/\tau < 16$ in vacuum at sufficient distance from the front and rear surface of the plasma layer, where only radiated fields exist. The broad emission line at $2\omega_p$ and also those at ω_p and $3\omega_p$ have been marked.

width of the plasmon peak $\Delta\omega/\omega_p \approx 0.3$ is set by the narrow time window $\Delta T/\tau = 3$. In addition to the plasmon peak, a broad excitation area around the laser frequency ω_0 is observed in Figure 10, which corresponds to the laser interaction at the surface during this time, and also smaller peaks at $2\omega_0$ and $3\omega_0$, corresponding to laser harmonics.

A very important result in the context of this article is found when shifting the time window to $6 < t/\tau < 12$. As one has already observed in Figure 9, then also left-bound plasma waves occur driven by reflected electron jets. In Figure 11 this leads to two plasmon peaks, again with $\omega \approx \omega_p$ and located more or less symmetrically at $k > 0$ and $k < 0$. Most of the excitation at multiples of the laser frequency have disappeared in Figure 11, because the laser pulse is switched off already at this later time. The plasmon peaks are narrower in the ω direction due to the longer time window when compared to Figure 10. On the other hand, the distribution in the k direction has broadened. This k broadening is a typical feature for large-amplitude Langmuir waves and is due to nonlinear interaction. Here it implies a mixture of phase velocities both larger and smaller than c and is of central importance to match the conditions for plasmon decay into photons.

Plasma radiation at multiples of ω_p is observed in the spectrum emerging from both sides of the plasma layer. The calculated spectrum in Figure 12 refers to the thin-layer case and the time window $9 < t/\tau < 12$. This limited time period, considered in the Fourier transform of the simulated electromagnetic field, leads to some additional broadening of the line structures in Figure 12 and is responsible for the emission seen at frequencies even below ω_0. The spectrum in Figure 12 shows a prominent emission peak at $\omega = 2\omega_p$ and weaker ones at $\omega = \omega_p$ and $\omega = 3\omega_p$. The $2\omega_p$ peak corresponds to a relative intensity of $a_{20}^2 = 2|E_y(2\omega_p)/E_0|^2 \Delta\omega/\omega_0 \approx 10^{-5}$. These emission peaks do not occur at early times ($t > 5\tau$). They are def-
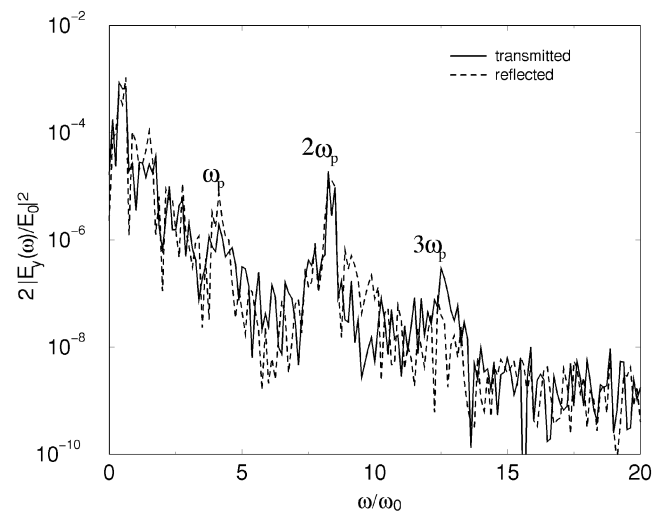
initely correlated with the appearance of counterpropagating plasma waves with two peaks in the k, ω plane, as they are observed in Figure 11.

We have varied the angle of incidence α of the driving external laser beam to find the optimum for conversion into $2\omega_p$ radiation. The emission curve is found to increase up to a peak at $\alpha \approx 55°$, the value used for the plots presented in this article. Beyond $\alpha \approx 55°$, the $2\omega_p$ emission drops sharply, and no emission is obtained for $\alpha > 60°$. The reasons for this becomes clear from the analytical treatment in the following.

5. ANALYTIC ESTIMATE OF SECOND HARMONIC EMISSION

In this section, we give an analytical derivation of the $2\omega_p$ emission by means of a second order expansion of Eqs. (4). The calculations are performed in the boosted 1D frame, and all quantities refer to the moving frame, but for notational convenience we have dropped the prime label. The only exception from this rule is the quantity ω_p, which is treated as an invariant parameter equal to the laboratory plasma frequency. In the boosted 1D system, we then find plasmons with frequency $\omega_{1,2} = \omega_p \cos\alpha$. Two plasmons can couple to a photon with frequency

$$\omega_T = \omega_1 + \omega_2 = 2\omega_p \cos\alpha \qquad (15)$$

and wave number

$$k_T = k_1 + k_2 = (2\omega_p/c)\sqrt{\cos\alpha^2 - \tfrac{1}{4}} \qquad (16)$$

according to the dispersion relation $\omega_T^2 = \omega_p^2 + (k_T c)^2$ derived in Section 2. Here the wave vectors k_T, k_1, k_2 in the boosted frame are actually x components and are equal to the x components in the laboratory frame [compare Eq. (3)]. Apparently, $\alpha = 60°$ is the largest angle, for which these photons of frequency $2\omega_p \cos \alpha$ can propagate in the layer.

Because the plasma waves are created at subliminal phase velocities and therefore $|k_{1,2}| > |k_T|$, the two plasmons have to move in opposite direction to satisfy Eq. (16). For $\alpha = 55°$ and $\omega_p/\omega_0 = \sqrt{18}$, we have $k_T/k_0 = 2.4$, where $k_0 = \omega_0/c$. Such a value of k_T is actually compatible with the distribution of wave vectors k_1 and k_2 in the simulation due to broadening seen in Figure 11. For the estimates below, we take $k_{1,2} \approx \omega_p/c$ from this plot.

In second order we find from Eqs. (4)

$$\left(\partial_x^2 - \frac{1}{c^2}\partial_t^2\right)a_{y2} = \left(\frac{\omega_p}{c}\right)^2 (a_{y2}\cos^2 \alpha - n_2 \tan \alpha + q_{2a}(x,t))$$

(17)

$$\partial_t^2 n_2 + \omega_p^2 n_2 = -c^2 \sin \alpha \cos \alpha \partial_x^2 a_{y2} + q_{2b}(x,t),$$ (18)

where the source terms are quadratic in the first-order solution (9) and are given by

$$q_{2a} = (\beta_{x1}^2/2)\tan \alpha + (3a_{y1}^2/2)\sin \alpha \cos^3 \alpha + n_1 a_{y1} \cos^2 \alpha$$

$$q_{2b} = (c^2/2)\partial_x^2 \beta_{x1}^2 - c\partial_x \partial_t(n_1\beta_{x1}) + c^2 \cos^2 \alpha(\tfrac{1}{2} - \sin^2 \alpha)\partial_x^2 a_{y1}^2$$

$$- c^2 \sin \alpha \cos^2 \alpha \partial_x(a_{y1}\partial_x \phi_1) - c \sin \alpha \cos \alpha \partial_x(\beta_{x1}\partial_t a_{y1}).$$

(19)

The wave equation for the photon amplitude a_{y2} can be brought into the form

$$\left[\partial_x^2 - \frac{1}{c^2}\partial_t^2 - \left(\frac{\omega_p}{c}\right)^2\right]a_{y2}(x,t) = \left(\frac{\omega_p}{c}\right)^2 q_2(x,t).$$ (20)

A complete expression for the source function $q_2(x,t)$ was derived by Lichters (1997). Here we collect only the two plasmon terms of the form $q_2(x,t) = q_0 \cos(\omega_T t - k_T x)$. For the amplitude q_0 we find after some algebra

$$q_0 = \frac{(4\cos^2 \alpha - 1)q_{2a,0} + (q_{2b,0}/\omega_p^2)\tan \alpha}{3\cos^2 \alpha},$$ (21)

with $q_{2a,0} = 0.39\phi_0^2$ and $q_{2b,0} = -0.066\omega_p^2\phi_0^2$, which are the corresponding amplitudes of the two source terms in Eq. (19), evaluated for $\alpha = 55°$, $k_p c/\omega_p \approx 1$, $k_T/k_p \approx 2.4$, $\omega_T/\omega_p \approx 1.15$. With these values, we obtain $q_0 \approx 0.022\phi_0^2 \approx 2 \times 10^{-3}$, taking the estimate $\phi_0 = (k_0/k_T)E_{x0}/E_0 \approx 0.1$ from Figure 9.

The solution of Eq. (20) is then obtained in the general form

$$a_{y2}(x,t) = \left(\frac{\omega_p}{c}\right)^2 \int_{-\infty}^{\infty} dx' g(x-x',t-t')q_2(x',t'),$$ (22)

using the Green function of the Klein–Gordon operator

$$g(x,t) = -\frac{c}{2}J_0\left(\omega_p\sqrt{t^2 - (x/c)^2}\right)\Theta(ct - |x|),$$ (23)

where J_0 denotes the Bessel function of first kind. In the present case, we find the amplitude of the right-going light wave at the right surface in the form

$$a_{20} = \frac{q_0}{2}\frac{1}{\sqrt{(\omega_T/\omega_p)^2 - 1}}\frac{\omega_p d}{c},$$ (24)

where d is the thickness of the foil. For $d = \lambda$, we find $\omega_p dc \approx 25$ and $a_{20} \approx 5 \times 10^{-3}$. Here we neglect effects of reflection and refraction at the boundaries, which are of order unity, and estimate the emission power at ω_T as $a_{20}^2 \approx 2 \times 10^{-5}$. This is in reasonable agreement with the value $a_{20}^2 \approx 10^{-5}$, obtained from the simulated $2\omega_p$ peak shown in Figure 12.

6. CONCLUSIONS

We conclude that ultrashort high-intensity laser pulses offer new possibilities to generate high-amplitude plasma waves and to study their interactions and decay into photons. The excitation of these waves is mediated by bunches of relativistic electrons (jets) accelerated by the laser light at the surface of a thin, overdense plasma layer and shot into the layer periodically with the laser frequency. The layer then starts to emit radiation at multiples of the plasma frequency. So far, this radiation has not been observed, but should be detractable with the intense few-cycle laser pulses now under development. The physical mechanism is analogous to the generation of solar type III radiation in the solar corona, and detection in laser experiments may provide new possibilities to study the astrophysical phenomenon in the laboratory.

The central result of this article is that this emission sets in only after counterpropagating plasma waves have been created. Those propagating opposite to the laser direction are driven by electron jets that have been reflected by strong space charge fields building up at the rear surface. In this article, we have studied the electron dynamics by 1D PIC simulation and have recovered the main feature of emission at plasma harmonics also analytically, solving the cold plasma equations in second-order perturbation theory.

A major limitation of the present work is the restriction to one-dimensional geometry, ignoring the fact that 2D and 3D effects like, for example, crater formation (Pukhov & Meyer-ter-Vehn, 1997) and current filamentation (Honda et al., 2000) can play a significant role in relativistic laser plasma interaction. Nevertheless, we believe that the present results give a correct description, at least qualitatively, for configurations in which the focal diameter is much larger than the layer thickness (thin layers) and ultrashort pulse durations of only a few laser cycles during which hole-boring effects can still be neglected. In view of the recent advances in

generating few-cycle laser pulses at ultrahigh intensities (Brabec & Krausz, 2000), one may expect that experimental studies will become possible in the near future. For the laser intensities of the order of 10^{18} W/cm^2 considered here, thin low-Z target layers will turn into dense plasma within the first laser cycle so that experiments may start from solid material.

The present results also indicate that the configuration of a single beam obliquely incident on a thin layer considered here may not be the best possible for generating the radiation at plasma harmonics. Making use of two laser beams incident from different directions and other target geometries, one may succeed in creating plasmons propagating at angles optimal for two-plasmon decay. Investigations of such options require at least 2D simulation. It is hoped that the present results will stimulate such work.

ACKNOWLEDGMENTS

REFERENCES

AAMODT, R.E. & DRUMMOND, W.E. (1964). *Plasma Phys.* **5**, 147.

BOURDIER, A. (1983). *Phys. Fluids* **26**, 1804.

BRABEC, T. & KRAUSZ, F. (2000). *Rev. Mod. Phys.* **72**, 545.

BRUNEL, F. (1987). *Phys. Rev. Lett.* **59**, 52.

HONDA, M., MEYER-TER-VEHN, J. & PUKHOV, A. (2000). *Phys. Rev. Lett.* **85**, 2128.

IVANOV, A.A. & RYUTOV, D.D. (1965). *Sov. Phys. JETP* **21**, 451.

LICHTERS, R. (1997). *Relativistische Wechselwirkung intensiver kurzer Laserpulse mit berdichten Plasmen: Erzeugung hoher Harmonischer*, Ph.D. thesis, Technical University of Munich, Germany.

LICHTERS, R., PFUND, R. & MEYER-TER-VEHN, J. (1997). *LPIC++: A Parallel One-dimensional Relativistic Electromagnetic Particle-In-Cell Code for Simulating Laser-Plasma Interaction*, Report MPQ-225, Max-Plank-Institut for Quantum Optics, Garching, Germany. Can be downloaded from http://www.mpq.mpg.de/library/mpq-reports.html#1997.

LICHTERS, R., MEYER-TEN-VEHN, J. & PUKHOV, A. (1998). *Superstrong Fields in Plasma* (Lontano, M. *et al.*, Eds.), *AIP Conf. Proc.* **426**, 41.

MELROSE, D.B., DULK, G.A. & CAIRNS, I.H. (1986). *Astronomy & Astrophysics* **163**, 229.

MOUROU, G. BARTY, C.P.J. & PERRY, M.D. (1998). *Phys. Today* **51**, 22.

PUKHOV, A. & MEYER-TER-VEHN, J. (1996). *Phys. Rev. Lett.* **76**, 3975.

PUKHOV, A. & MEYER-TER-VEHN, J. (1997). *Phys. Rev. Lett.* **79**, 2686.

REMINGTON, B.A., DRAKE, R.P., ARNETT, D. *et al.* (2000). Astrophys. J. Suppl. Series 127, 211.

RYUTOV, D.D. (1966). *Sov. Phys. Doklady* **10**, 968.

RYUTOV, D.D., REMINGTON, B.A. & ROBEY, H.F. (2001). *Phys. Plasmas* **8**, 1804.

STRICKLAND, D. & MOUROU, G. (1985). *Opt. Comm.* **56**, 219.

TATARAKIS, M. *et al.* (2002). *Nature* **415**, 280.

TEUBNER, U., ALTENBERND, D., GIBBON, P., FÖRSTER, E., MYSYROWICZ, A., AUDEBERT, P., GEINDRE, J.-P., GAUTHER, J.C., LICHTERS, R. & MEYER-TER-VEHN, J. (1997). *Opt. Comm.* **144**, 217.

VASQUEZ, A.M., GOMEZ, D.O. & FONTÁN, C.F. (2002). *Astrophys. J.* **564**, 1035.

VYACHESLAVOV, L.N., BURMASOV, V.S., KANDAUROV, I.V., KRUGLYAKOV, É.P., MESHKOV, O.I. & SANIN, A.L. (2002). *JETP Lett.* **75**, 41.